



Boosting oxygen reduction reaction with Fe and Se dual-atom sites supported by nitrogen-doped porous carbon

Zhaoyang Chen^a, Xiaozhi Su^b, Jie Ding^a, Na Yang^{c,*}, Wenbin Zuo^d, Qinye He^a, Zhiming Wei^a, Qiao Zhang^a, Jian Huang^a, Yueming Zhai^{a,*}

^a The Institute for Advanced Studies, Wuhan University, Wuhan 430072, China

^b Shanghai Synchrotron Radiation Facility, Shanghai Advanced Research Institute, Chinese Academy of Sciences, Shanghai 201204, China

^c School of Information and Optoelectronic Science and Engineering, South China Normal University, Guangzhou 510006, China

^d Key Laboratory of Artificial Micro and Nanostructures of Ministry of Education, Hubei Key Laboratory of Nuclear Solid Physics, School of Physics and Technology, Wuhan University, Wuhan 430072, China

ARTICLE INFO

Keywords:

Dual-atomic-site catalysts

Single-atom catalysts

Spin-state

Oxygen reduction reaction

ABSTRACT

Dual-atomic-site catalysts (DASCs), as an extension of single-atom catalysts (SACs), have attracted increasing attention owing to the synergistic effect. However, the study of DASCs is still at the early stages and mainly based on metal atom pairs. More experimental and theoretical exploration needed for further guiding the reasonable design of diatomic active sites. Herein, remarkable activity for oxygen reduction reaction (ORR) of Se₁-NC single-atom catalyst was discovered, and then Fe/Se dual-atom catalysts were constructed to demonstrate the dual-atom sites synergistic effect. Encouraging, the Fe₁Se₁-NC catalyst displays significant enhancement for ORR towards Fe₁-NC and Se₁-NC in both alkaline and acid electrolytes. Spectroscopic characterizations and theoretical calculations reveal that there are multiple effects for the introduction of Se, especially for supplying new active sites, and effectively tuning charge redistribution and the spin-state of Fe active sites, which presenting a new strategy to improve the electrochemical performance based on the metal-nonmetal dual-atomic-site catalysts.

1. Introduction

Metal-air batteries and fuel cells are promising next-generation renewable energy devices due to their high energy density and zero carbon emissions features [1–5]. However, the practical maturity of these devices has been severely obstructed by oxygen reduction reaction (ORR) occurring at the cathodic. Through the ages, platinum (Pt)-group catalysts exhibit outstanding O₂ reduction abilities, but the high price and natural scarcity hamper their large-scale applications [6–10]. Dai et al. reported the enhanced ORR activity of nitrogen-doped carbon nanotubes due to abundant defects [11]. However, metal-free catalysts often show limited activity and poor stability especially in acidic media. In contrast, introducing of transition metal (Fe, Co and Mn etc.) into nitrogen doped carbon (M-N-C) have been demonstrated as an effective way for improving ORR activity [12–17]. In recent years, single-atom catalysts (SACs) attract increasing attentions owing to their fully exposed active sites and also providing simple model catalysts for the reaction mechanism investigation [18–22]. Among the studied

transition metal-based catalysts, Fe-NC, especially composed of monatomic Fe, is hailed as the most promising candidate towards Pt/C substitution.

However, recent researches have pointed out that single atom catalyst also meet some drawbacks [23–27]: (1) Hard to break the severe limitation of scale relationship on catalytic activity. (2) Serious deactivation often happened on single-atomic-site catalysts owing to low density of active sites which are easily occupied by intermediates. (3) Single active center unable to efficiently drive the multielectron and multiproton transfer procedure. To address these problems, introducing of other single atom to construct heteronuclear diatoms may endow catalyst higher turnover frequency. This strategy probably has great potential to overcome these shortcomings, and finally enhanced activity through tunable electronic environments and geometry configuration. Furthermore, the modular design of catalyst may be finally achieved by reasonably utilizing atomic building blocks. In 2017, Li et al. developed a host-guest strategy to construct Fe-Co dual-atom sites on N-doped porous carbon for ORR [28]. Subsequently, researchers also found

* Corresponding authors.

E-mail addresses: yangna@m.scnu.edu.cn (N. Yang), yueming@whu.edu.cn (Y. Zhai).

<https://doi.org/10.1016/j.apcatb.2022.121206>

Received 20 December 2021; Received in revised form 25 January 2022; Accepted 9 February 2022

Available online 11 February 2022

0926-3373/© 2022 Elsevier B.V. All rights reserved.

AuCo, FeMn and CuZn diatomic catalysts exhibiting enhanced ORR activity compared to single metal active site catalysts [29–31]. In the past, researchers have often focused on construction of metal atom pair catalysts and few reports combined metals and non-metals together. Metals and non-metals often exhibit different physical and chemical properties, and bringing the two types of atoms together could provide different roles in the catalytic reaction. Selenium atoms, possessing rich d -electron and high electrical polarizability, have been confirmed to significantly enhance the electron transport efficiency of two dimension materials [32,33]. Here, we synthesized atomically dispersed Fe and Se dual atoms anchored on nitrogen-doped carbon through a ball-milling strategy. X-ray absorption near-edge structure (XANES) and extended X-ray absorption fine structure (EXAFS) analysis indicated that this catalyst mainly contains unsymmetrical coordination Fe-N₅ moiety and SeC₂ dual sites. Interestingly, besides Fe₁-NC, it is found that Se single atom sites also exhibited remarkable activity for ORR, and the dual-atomic-site catalysts showed a significantly enhanced activity in both acid and alkaline condition towards the single counterpart. ⁵⁷Fe Mössbauer spectroscopy identified that both low spin (LS) Fe³⁺ and medium-spin (MS) Fe²⁺ exist in these catalysts. Significantly, adding Se atoms into the catalyst could enhance the content of LS polarization configuration of Fe, which is favorable for enhancing the adsorption strength of ORR intermediate and improving the electroconductibility [34,35]. Meanwhile, correlational research also reveal that MS Fe(II)N_x has excellent stability [36]. Density functional theory (DFT) calculations and ab initio molecular dynamics (AIMD) calculations further revealed that the enhanced activity attributed to the moderate reaction Gibbs free energy of ORR intermediate on dual active sites, which is beneficial to improve the kinetic process of ORR. Overall, the introducing of Se atomic sites has several functions: (1) It can adjust the electronic state and spin structure of the Fe-N_x active site to reduce the activation energy barrier of the rate-determining step. (2) The Se-C₂ can also serve as active ORR reaction site. (3) Due to the relative low sublimation temperature of SeO₂ (~315 °C), most of it will be volatilized during the calcination process, which will leave rich pore structure on the catalyst. The porous structure is more conducive to the mass transfer. This work not only demonstrates that constructing Fe/Se dual-atomic-site catalysts could enhance the activity of ORR by multiple effects, but also provides a unique insight of atomically introducing of non-metal active sites for rational design of more effective catalysts.

2. Experimental section

2.1. Reagents

All chemicals including melamine (99%), L-alanine (99%), Selenium dioxide, hydrochloric acid (37%), Iron trichloride hexahydrate, Potassium hydroxide (90%) were purchased from adamas-beta and used directly without further purification. Nafion® 117 solution (~5% in a mixture of low aliphatic alcohols and water) were purchased from Sigma-Aldrich. Deionized water from Millipore Q water purification system was used to make the solutions.

2.2. Catalyst preparation

In a typical synthesis of Fe₁Se₁-NC, 6 g melamine, 1.5 g L-alanine, 3.0 g SeO₂ and 5 mg Iron trichloride hexahydrate were first ground into a homogeneous precursor by ZrO₂ mortar ball for 2 h. Following, 10 mL mixed solution of ethanol and hydrochloric acid (volume ratio 5:1) was added. The slurry continue to grind until the ethanol was evaporated. The mixture was dried in an oven at 80 °C and ball milled again for 20 min. Subsequently, the fine powder mixture was undergone a two-stage pyrolysis and carbonization process at the N₂ atmosphere (first stage: from 25 °C to 550 °C, maintain at 550 °C for 2 h and then heated to 900 °C for 90 min). The heating rate of the whole process at a rate of 2 °C/min. The same method was used for the synthesis of Fe₁-NC, NSC,

and NC (For Fe₁-NC, no SeO₂ was added and 7 mg Iron trichloride hexahydrate added towards Fe₁Se-NC; SeNC, no metal salt was added towards Fe₁Se₁-NC; NC, no metal salt was added towards Fe₁-NC).

2.3. Material characterizations and electrochemical measurements

The crystal structure of the products was determined by powder X-ray diffraction (XRD, Smartlab SE, Japan). The surface morphologies were observed by field emission scanning electron microscopy (Zeiss SIGMA) and transmission electron microscopy (TEM, JEOL plus-2100, Japan). X-ray photoelectron spectroscopy (XPS) tests were performed utilizing a Thermo Fischer ESCALAB 250Xi spectrophotometer. All binding energies were referenced to the C 1s peak (284.6 eV). Raman spectroscopy was measured with the Raman microscope (JY-HR800, λ excited=532 nm). The specific surface area and the pore size distribution of products were determined by Brunauer-Emmett-Teller (BET) method (Quantachrome Instruments, USA). The thickness of the nanosheets was determined by atomic force microscope (AFM, Bruker-Icon SPM). Sub-ångström-resolution HAADF-STEM characterization was conducted with a JEOL JEMARM200F STEM/TEM instrument with a resolution of 0.08 nm. The X-ray absorption spectra (XAS) including X-ray absorption near-edge structure (XANES) and extended X-ray absorption fine structure (EXAFS) of the samples at Fe K-edge were collected at the BL 14W1 of Shanghai Synchrotron Radiation Facility (SSRF) in China. A double Si (111)-crystal monochromator was used for energy selection. Fe foil was employed to calibrate the energy. The spectra were collected at transmission mode at room temperature. Athena software package was used to analyze the data. The Mössbauer measurements were performed at room temperature using a conventional spectrometer (Germany, Wissel MS-500) in transmission geometry with constant acceleration mode. A ⁵⁷Co (Rh) source with activity of 25 mCi was used. The velocity calibration was done with a room temperature α -Fe absorber. The spectra were fitted by the software Recoil using Lorentzian Multiplet Analysis[37].

2.4. Electrochemical measurements

The Electrochemical measurements were performed on CHI 660 electrochemical workstation (CHI Instruments Inc.) and Autolabpotentiostat (PGSTAT302N) system coupled with a Pinerotator (AFMS-LXF) in a three-electrode system with Ag/AgCl as reference electrode and carbon rod as counter electrode. Linear sweep voltammograms (LSV) were measured using glass carbon rotating disk electrode (RDE, 5.0 mm diameter) as a working electrode. The modified electrode was prepared as follows: put 5 mg samples in 1 mL of ethanol-water mixed solution (the volume ratio of ethanol and water is 1:1) under ultrasonic for 30 min, the catalyst dispersion was dropped onto RDE electrodes (8 μ L). After drying at room temperature, it was coated with a thin film of 0.5% Nafion solution. Before modification, the glassy carbon electrode and RRDE electrode was polished by 0.3 and 0.05 μ m alumina powder to form mirror-like surface. The electrode was then sonicated in ethanol and deionized water with a volume ratio of 1:1, and then the electrode was dried at room temperature.

Koutecky-Levich (K-L) equations:

$$J^{-1} = J_L^{-1} + J_K^{-1} = (B\omega/2)^{-1} + J_K^{-1} \quad (1)$$

$$B = 0.62nFC_0(D_0)^{2/3}\nu^{-1/6} \quad (2)$$

where J is the measured kinetic density, J_k is the kinetic current density, .

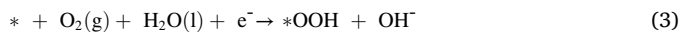
J_d is the diffusion-limiting current density, ω is the angular velocity of the disk in rad s⁻¹ ($\omega = 2\pi N/60$, N = rotation speed in rpm), F is the Faraday constant (96485 C mol⁻¹), D is the diffusion coefficient of O₂ in the electrolyte (1.90 $\times 10^{-5}$ cm² s⁻¹), ν is the kinematic viscosity of the electrolyte (0.01 cm² s⁻¹), C_0 is the bulk concentration of O₂ in the electrolyte (1.20 $\times 10^{-6}$ mol cm⁻³).

2.5. Computational details

Our computational simulations were performed by Vienna ab-initio simulation package (VASP) with the projector augmented wave pseudo-potentials (PAW) to describe the interaction between atomic cores and valence electrons with density functional theory (DFT+U) [38,39]. The Perdew–Burke–Ernzerhof (PBE) functional within the generalized gradient approximation (GGA) were used to implement DFT calculations [40]. The Fe₁-NC and Fe₁Se₁-NC slab models were employed to simulate the surface properties. The reasonable vacuum layers were set around 15 Å in the z-direction for avoiding interaction between planes. A cutoff energy of 500 eV was provided, $2 \times 2 \times 1$ Monkhorst Pack k-point sampling were chosen for the well converged energy values of slab models. Geometry optimizations were pursued until the force on each atom falls below the convergence criterion of 0.02 eV/Å and energies were converged within 10^{-5} eV. Furthermore, we applied DFT+U through the rotationally invariant approach with the corresponding U-J value (U-J)Fe= 3.29) [41]. To explore the interaction between the Fe and N atom, we conducted a projected density of states (PDOS) analysis and implemented in the DS-PAW code [42]. Moreover, all calculations were spin polarized.

Dynamic optimized configuration temperature and total energy change for system at 400 K within 10 ps during AIMD simulation. To reduce the computational cost, the hydrogen mass was increased to 2 at. mass unit (H/D-exchange), timestep set as 1 fs, and the temperature was controlled by using the canonical ensemble (NVT) and Nosé–Hoover thermostat method [43]. Moreover, all calculations were spin polarized.

In this work, the ORR 4e⁻ pathway is as follows:



where symbol * represents the Fe active site in the specific catalyst surface, and (l)/(g) represents the liquid/gas phase of various intermediate species. $\Delta G = \Delta E + \Delta \text{ZPE} - T\Delta S + \Delta G_{\text{U}} + \Delta G_{\text{pH}}$ be defined as the value of free energy change of 1–5 steps, where ΔE is the reaction energy of reactant and product molecules adsorbed on catalyst surface. ΔZPE is the zero point energy difference, $T\Delta S$ is the entropy change, and $T = 298$ K. $\Delta G_{\text{U}} = -eU$, U is the potential measured versus reversible hydrogen electrode (RHE) at standard conditions and e is the elementary charge. $\Delta G_{\text{H}^+}(\text{pH}) = -k_{\text{B}}T \ln(10) \times \text{pH}$, here, $\text{pH} = 0$, and $\Delta G_{\text{pH}} = 0$.

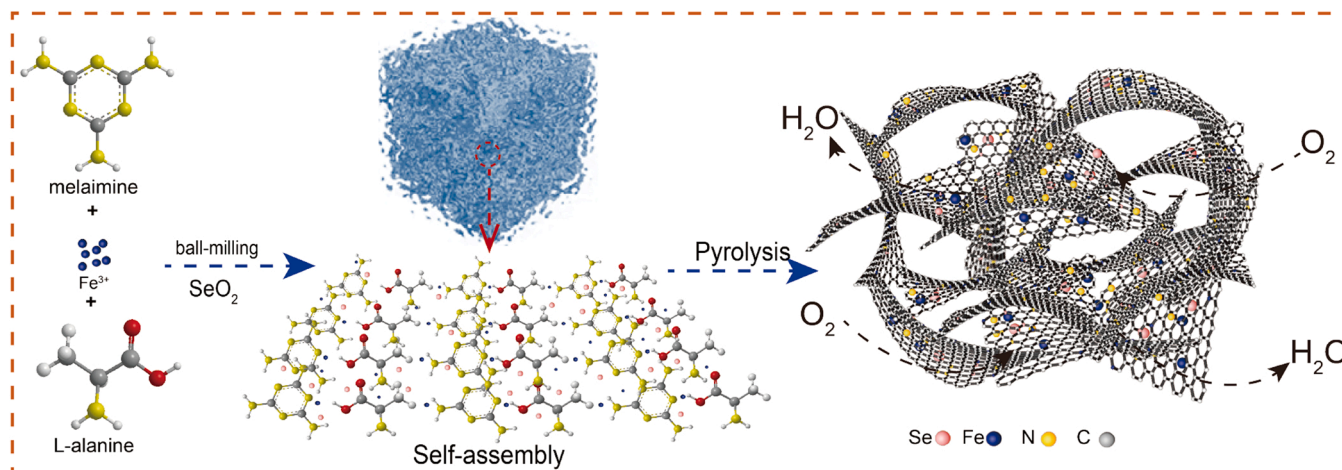
3. Results and discussion

3.1. Catalyst preparation and structure characterization

In a typical experiment, the target catalyst Fe₁Se₁-NC was synthesized by grinding melamine, L-alanine, FeCl₃ and SeO₂ into a homogeneous precursor (Scheme 1), followed by a two-step high-temperature calcination under nitrogen atmosphere (see experimental section for details). Fe₁-NC catalyst was prepared without adding SeO₂. The catalysts without metal synthesized for comparison are denoted as Se₁-NC and NC.

These four catalysts only display (002) plane of graphitic carbon with diffraction peak at 26.2° and diffraction peak at 43.6° of the (101) plane for typical amorphous carbon by X-ray diffraction (XRD) characterization (Fig. 1A). No other diffraction peak of Fe-based species is detected in both Fe₁Se₁-NC and Fe₁-NC samples. Compared with Fe₁-NC and NC, the peaks for Fe₁Se₁-NC and Se₁-NC become broader and weaker, suggesting that the additional Se doping could result in low crystallinity and defective structure [44], which was further proved by a higher $I_{\text{D}}/I_{\text{G}}$ ratio of Fe₁Se₁-NC by Raman spectroscopy (Fig. S1). The measured specific surface area of the Fe₁-NC and Fe₁Se₁-NC are 262 m²g⁻¹ and 422 m²g⁻¹ respectively (Fig. S2). The increase of specific surface area about Fe₁Se₁-NC is mainly due to the relative low sublimation temperature of SeO₂, a large proportion will be volatilized during the calcination process and leave rich pore structure on the catalyst. Corresponding pore size distributions curve indicate both micropores (0–2 nm) and mesopores (3–8 nm) co-exist in this catalyst. Such large surface area is beneficial to reactant penetration and small pores could also serve as electron acceptors for various electron-donating guest species [45]. The typical morphology of Fe₁Se₁-NC is flexible, sheet-like thin layer and no obvious nanoparticles could be visualized (Fig. 1B–C). Atomic force microscopy (AFM) analysis (Fig. 1B inset) further confirms the two-dimensional structure and the thickness is around ~1.2 nm. Such ultra-thin structure is more conducive to the exposure active sites. Moreover, the elemental mapping of Fe₁Se₁-NC (Fig. 1D) revealed the uniform distribution of C, N, Se and Fe elements on the carbon. All of the above results suggest that the Fe or Se species are probability dispersed as single atoms. The actual content of Fe was measured by ICP-OES (1.8% for Fe₁Se₁-NC). The catalysts were further characterized by aberration-corrected high angle annular dark field scanning transmission electron microscopy (HAADF-STEM). In Figs. 1E and 1F, bright dots assigned to single Se atom and Fe/Se dual atoms distributed across the entire sample region respectively. More morphology analysis of the Fe₁-NC, Se₁-NC and NC are shown in Fig. S3 to S5.

A series of spectroscopy techniques were performed to clarify the



Scheme 1. Schematic illustration displaying the preparation process of Fe₁Se₁-NC.

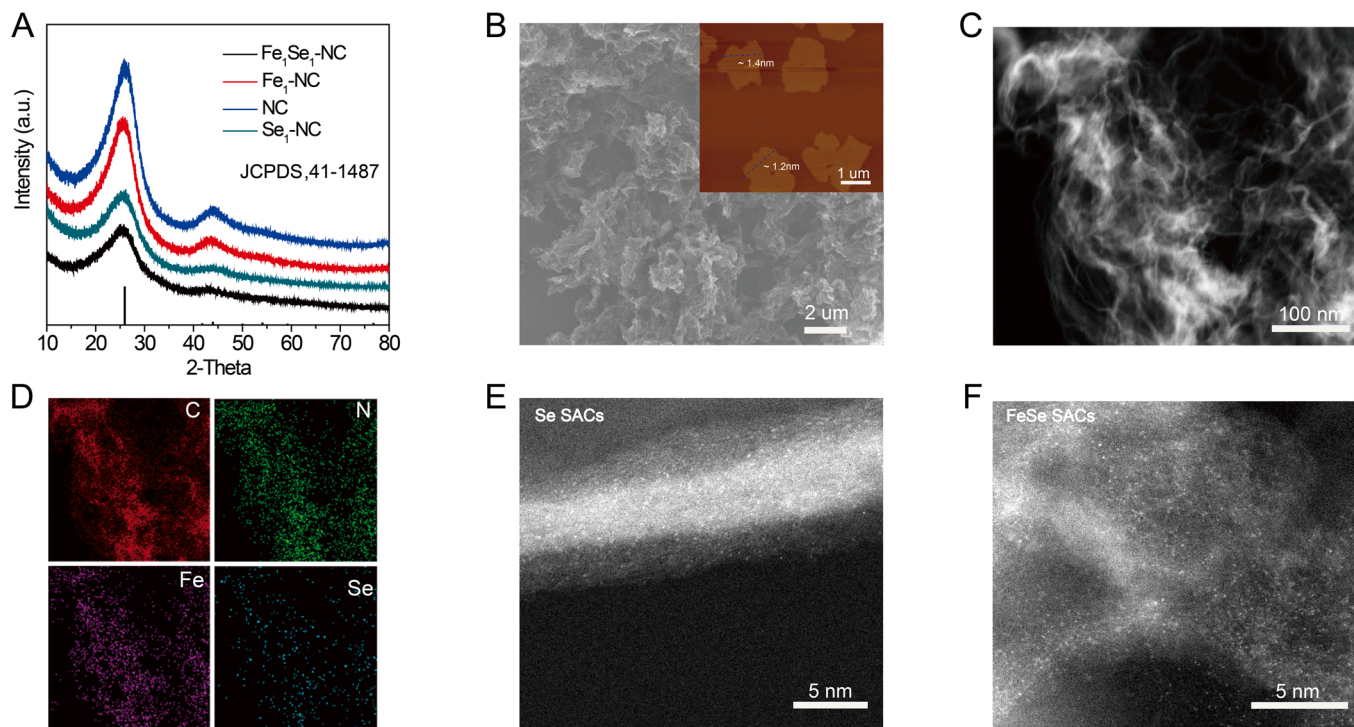


Fig. 1. Structural characterization of catalysts. A, X-ray diffraction patterns. B, SEM and AFM images (inset) of Fe₁Se₁-NC. C and D, STEM image and corresponding EDX elemental mappings of Fe₁Se₁-NC. E, Aberration-corrected STEM images of Se₁-NC. F, Aberration-corrected STEM images of Fe₁Se₁-NC.

binding states and coordination structure of the studied catalysts. In Fig. S6, the high-resolution XPS spectrum of N1s indicates four N species exist, including pyridinic N (~ 398.3 eV), Fe-N (~ 399.1 eV), graphitic N (~ 401.0 eV) and oxidized N (~ 402.3 eV) species [46]. Se 3d XPS

spectrum reveals a main peak at 55.9 eV can be assigned to C-Se-C units (Fig. S6B) [47]. Fig. S6A display the Fe 2p XPS spectrum and the peaks at 709.8 and 712.8 eV correspond to the 2p_{3/2} orbitals of Fe (II) and Fe (III) species. While the peaks at 722.6 and 728.3 eV are correspond to the

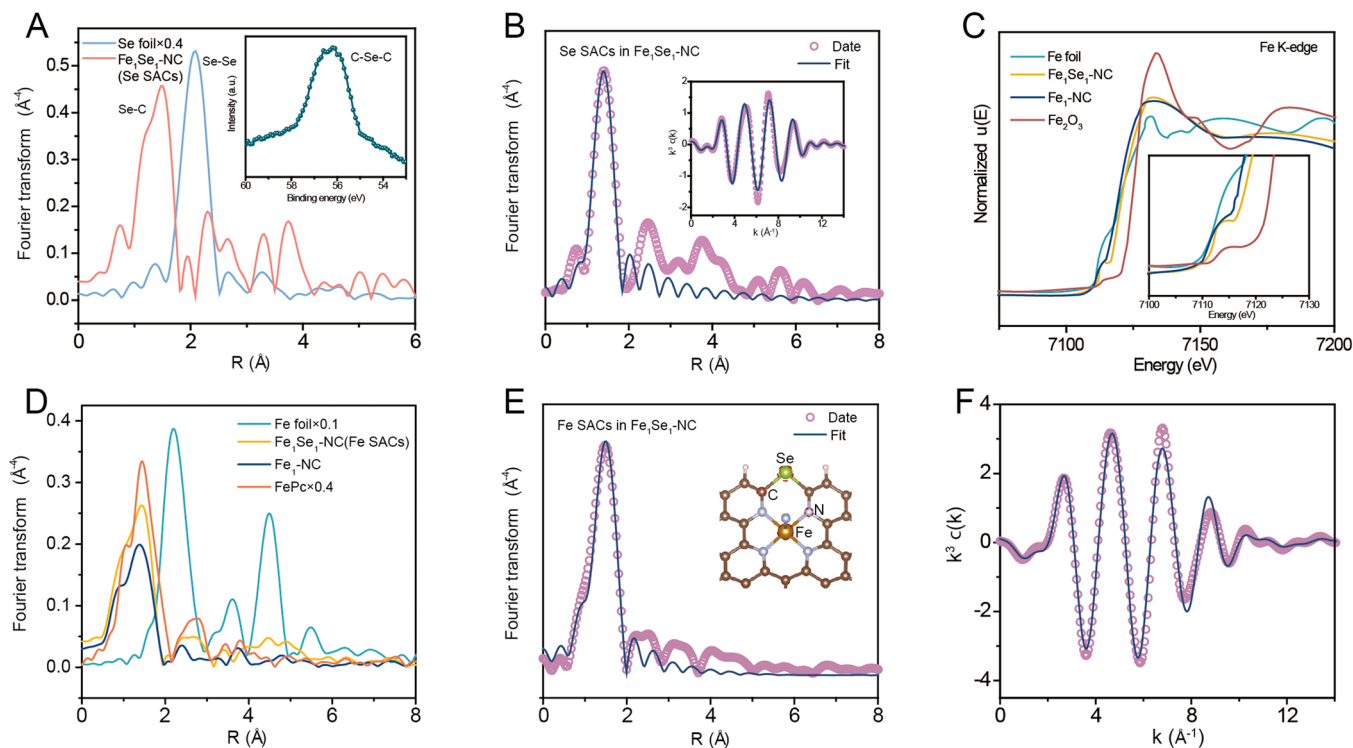


Fig. 2. Local electronic states of the catalysts. A, Se K-edge Fourier-transformed EXAFS spectra of Fe₁Se₁-NC (inset shows the XPS spectra of Se 3d). B, Fitting curves of the EXAFS of Se SACs of Fe₁Se₁-NC in the R-space and K-space (inset of B). C, The experimental Fe K-edge XANES spectra of Fe₁Se₁-NC, Fe₁-NC and the references (Fe foil and Fe₂O₃). D, Fe K-edge Fourier transformed EXAFS spectra in the R space. E and F, Fitting curves of the EXAFS of Fe SACs of Fe₁Se₁-NC in the R-space and K-space.

$2p_{1/2}$ orbitals of Fe (II) and Fe (III) peaks, respectively. The Fe species in $\text{Fe}_1\text{Se}_1\text{-NC}$ and $\text{Fe}_1\text{-NC}$ are in an intermediate oxidation state with Fe (II) and Fe (III), respectively (Fig. S7) [48]. We have compared the XPS spectra of N 1 s and C 1 s between $\text{Fe}_1\text{Se}_1\text{-NC}$ and $\text{Fe}_1\text{-NC}$ after fitting. As shown in Fig. S7, the overall composition ratio does not change significantly after the introduction of Se. However, the binding energies of N 1 s and C 1 s are positively shifted to the high-energy direction after the introduction of Se. The doped Se atoms facilitate electron transfer from C or N to Se. The XPS spectrum of $\text{Fe}_1\text{-NC}$, $\text{Se}_1\text{-NC}$ and NC after fitting are supplied in Fig. S7. Furthermore, X-ray absorption fine structure (XAFS) measurements were further carried out to probe the valence state and local structural information [49–51]. In Fig. 2A, the Fourier-transformed (FT) k^3 -weighted EXAFS spectrum in R-space revealed a primary peak at 1.40 Å assigned to Se-C scattering path in the first coordination shell, and the Se-Se bond (2.07 Å) was absent. This result suggests single atom Se exist in the resultant $\text{Fe}_1\text{Se}_1\text{-NC}$ catalyst. The EXAFS fitting curves shows that the coordination number in the first coordination shells are 2.0. Furthermore, the corresponding interatomic distance is 1.85 Å (Fig. 2B). Similarly, the oxidation state and coordination structure of the iron species were also characterized by XANES and EXAFS. In Fig. 2C, the normalized XANES spectra of $\text{Fe}_1\text{Se}_1\text{-NC}$ and $\text{Fe}_1\text{-NC}$ were compared with several standard samples. The absorption

edge position of $\text{Fe}_1\text{Se}_1\text{-NC}$ and $\text{Fe}_1\text{-NC}$ are located between Fe foil and Fe_2O_3 , suggesting that the average valence state of Fe is between the two references. The Fourier-transformed (FT) EXAFS spectra of $\text{Fe}_1\text{Se}_1\text{-NC}$ and $\text{Fe}_1\text{-NC}$ in Fig. 2D displayed one strong peak at 1.5 Å, which is assigned to Fe-N scattering path. Notably, no related peak corresponding to Fe-Fe bond at 2.2 Å was observed in both $\text{Fe}_1\text{Se}_1\text{-NC}$ and $\text{Fe}_1\text{-NC}$, suggesting the presence of individually distributed Fe in our studied catalysts. The result of XAFS is in consistent with the HAADF-STEM observing. The fitting curves display in Fig. 2E and Table S1, which uncover that the coordination number of Fe atom is around 5 and bond length is about 2.02 Å and 2.0 Å for $\text{Fe}_1\text{Se}_1\text{-NC}$ and $\text{Fe}_1\text{-NC}$, respectively.

Based on above results, in order to simulate the structural stability

using the simplified models, herein, we firstly ignored the edge and vacancy on models. As shown in Figs. 3A and 3B, we built the $\text{Fe}_1\text{Se}_1\text{-NC}$ and $\text{Fe}_1\text{-NC}$ models, in which, NH_2 species was used for axial coordination on Fe site to satisfy 5 coordination number in the first shell of Fe center [52]. The ab initio molecular dynamics (AIMD) simulations were utilized to elucidate the stability of $\text{Fe}_1\text{Se}_1\text{-NC}$ and $\text{Fe}_1\text{-NC}$ models. The results suggest that FeN_5 active sites on $\text{Fe}_1\text{-NC}$ and $\text{Fe}_1\text{Se}_1\text{-NC}$ maintain a good configuration undergoing 10 ps AIMD process at 400 K in implicit solvation, indicating that this structure exhibits excellent dynamic stability during the fuel cells operation ($T < 400$ K).

3.2. ORR catalytic activity

The ORR performances of the resultant catalysts were evaluated by the three-electrode configuration on a rotating disk electrode (RDE) apparatus in both alkaline and acid solutions. Over the whole testing process, carbon rod was used as the counter electrode. The cyclic voltammetry (CV) test of the $\text{Fe}_1\text{Se}_1\text{-NC}$ catalyst was carried out under the conditions of oxygen or argon saturation, respectively (Fig. S8). Notable reduction peaks can be seen under the oxygen saturation, while no peak appeared under argon conditions, which showed that $\text{Fe}_1\text{Se}_1\text{-NC}$ catalyst possessed excellent ORR ability. Fig. 4A displays the LSV curves in alkaline solution, $\text{Fe}_1\text{Se}_1\text{-NC}$ catalyst shows the highest activity in view of the onset potential (E_{onset}) of 1.0 V vs. RHE. This value is superior to Pt/C (0.98 V), $\text{Fe}_1\text{-NC}$ (0.95 V), and $\text{Se}_1\text{-NC}$ (0.95 V). The resultant $\text{Fe}_1\text{Se}_1\text{-NC}$ catalyst also shows the highest kinetic current density ($J_k = 5.89 \text{ mA cm}^{-2}$) and half-wave potential ($E_{1/2} = 0.88$ vs. RHE) among the studied catalysts (Fig. 4G left). Notably, compared with NC, the introduction of Se single atom sites greatly improves the oxygen reduction activity, suggesting it also can serve as ORR active site. The accelerated cyclic voltammetry test was applied to appraise the durability of $\text{Fe}_1\text{Se}_1\text{-NC}$. As shown in Fig. 4B, $\text{Fe}_1\text{Se}_1\text{-NC}$ only exhibits 13 mV negative shifts of the $E_{1/2}$ after 5000 continuous cycles. To further understand the ORR mechanism and electron transfer number in ORR,

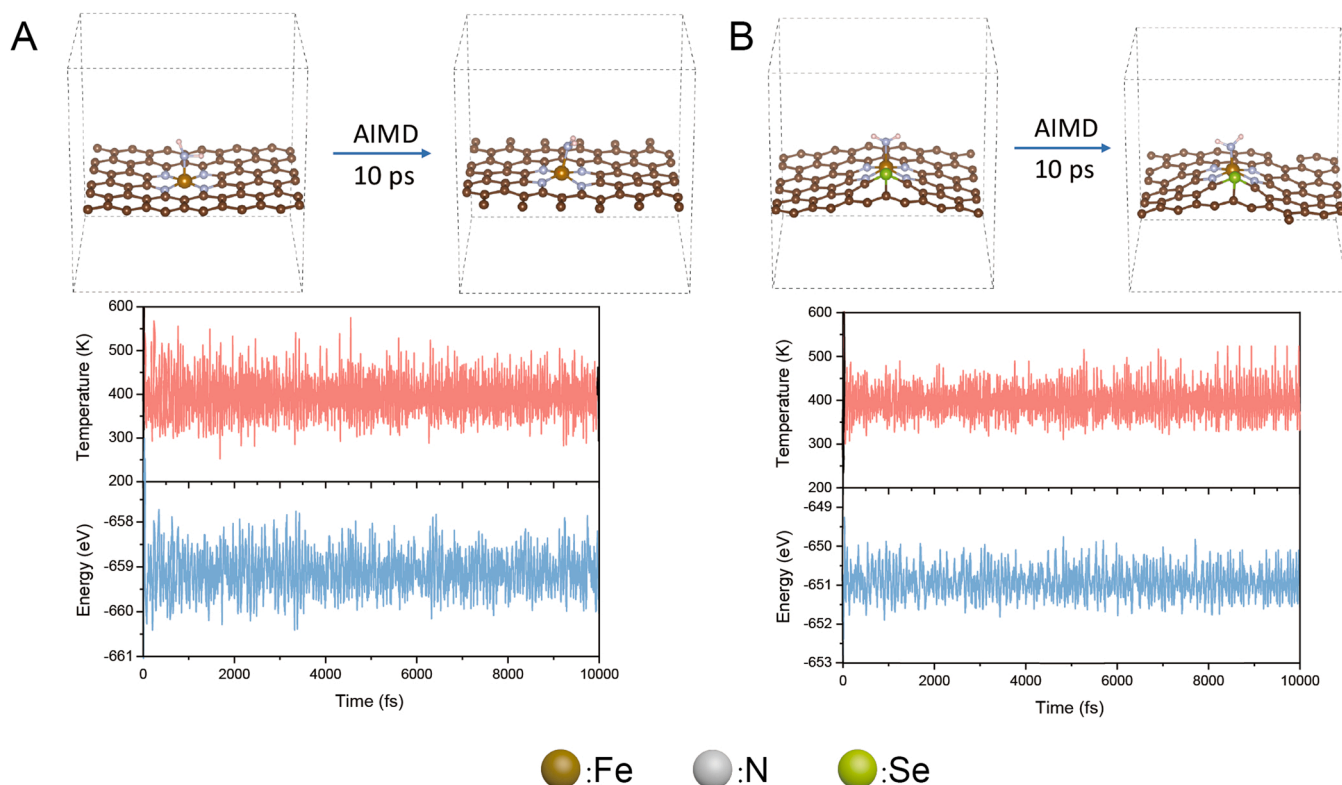


Fig. 3. A and B, Dynamic optimized configuration snapshot total energy and temperature for $\text{Fe}_1\text{-NC}$ and $\text{Fe}_1\text{Se}_1\text{-NC}$ at 400 K within 10 ps AIMD simulation. The temperature was controlled by using the Nosé-Hoover method.

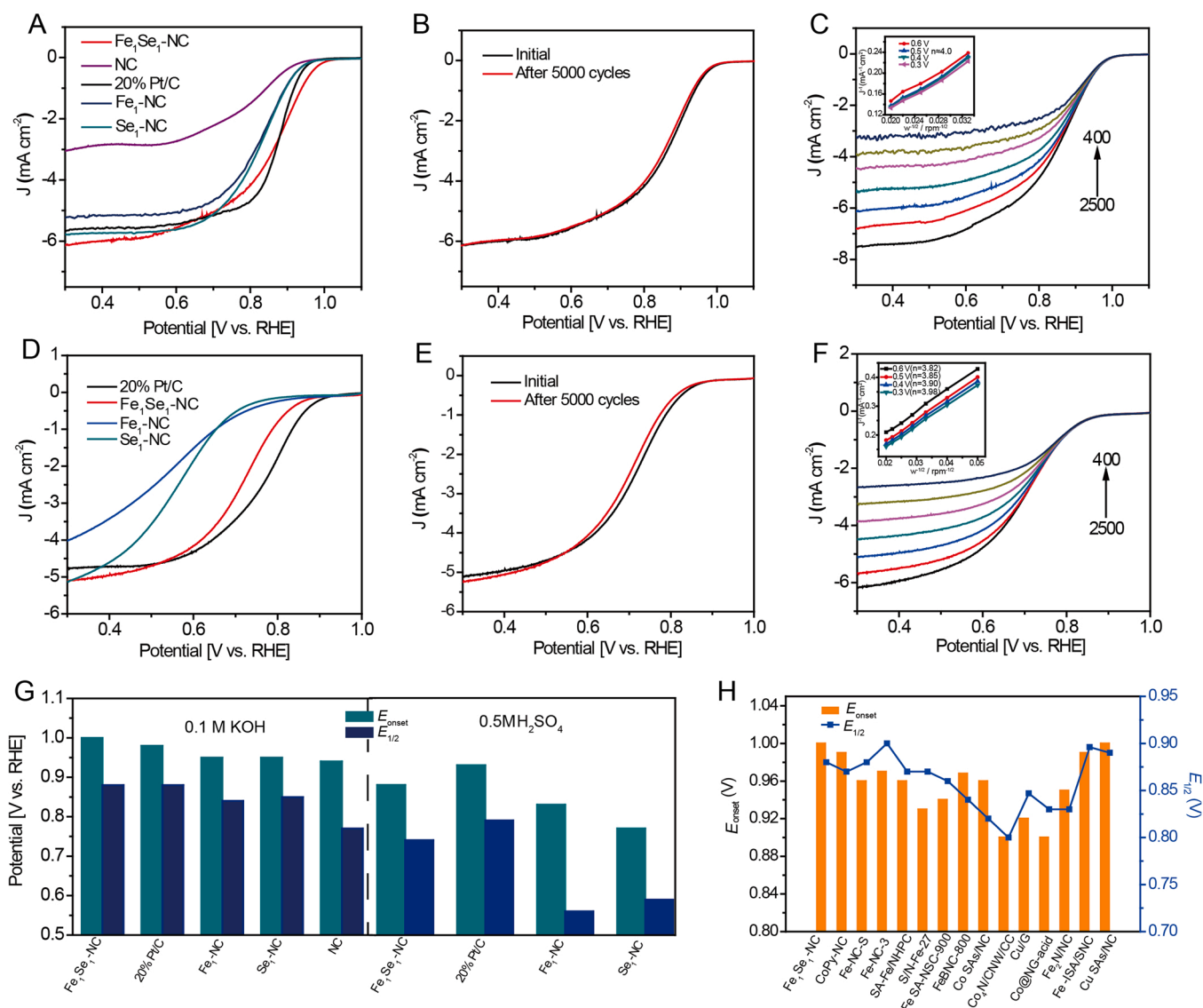


Fig. 4. ORR performances. A, LSV curves for the catalysts acquired in O₂-saturated 0.1 M KOH solution on a rotating disc electrode(RDE) at 1600 rpm and a scanning rate of 5 mV s⁻¹. B, Long-term durability measurement of Fe₁Se₁-NC, before and after 5000 cycles. C, Polarization curves at various rotation rates and corresponding K-L plots. D, LSV curves for the catalysts acquired in O₂-saturated 0.5 M H₂SO₄ solution. E, Long-term durability measurement of Fe₁Se₁-NC. F, Polarization curves at various rotation rates and corresponding K-L plots. G, The contrast between Fe₁Se₁-NC and the references for J_k and $E_{1/2}$. H, Contrasting the E_{onset} and $E_{1/2}$ values for Fe₁Se₁-NC and the catalysts in literatures.

different rotating speed test was applied by rotating disk electrode (RDE) (Fig. 4C). The diffusion current densities enhanced as the rotation speed increased, which can be attributed to the fact that oxygen molecular accelerated diffusion to the electrode surface from the electrolyte. The Koutecky-Levich (K-L) plots show good linearity and the slope remain basically unchanged, indicating that the reaction is a first order ORR reaction kinetics [53]. The corresponding electron transfer number (n) was calculated to be ~ 4.0 , demonstrating an ideal reduction process of O₂ to OH⁻ by a direct four-electron ORR pathway (Fig. 4C inset). Additionally, the enhancement of ORR activity of non-noble metal catalyst in acid medium is more.

meaningful towards in alkaline electrolytes. Thus, we examined the ORR performance in 0.5 M H₂SO₄ solution. As seen from the LSV plots (Fig. 4D and Fig. 4G right), the ORR activity of Fe₁Se₁-NC is much higher than Fe₁-NC and Se₁-NC. Compared to Pt/C, only 50 mV gap of the $E_{1/2}$ exists. We also investigate the durability of Fe₁Se₁-NC in acid medium. A negligible attenuation about 13 mV in $E_{1/2}$ was observed after 5000 cycles. Similar to that in alkaline electrolyte, Fe₁Se₁-NC in acid medium also displays a 4e⁻ reaction process and the n value is about

3.82–3.98. All above results confirm that Fe₁Se₁-NC possess excellent catalytic activity and synergistic effect exists between the two active sites. Different rotating speeds of LSV curves about Fe₁-NC, Se₁-NC and NC in both alkaline and acidic conditions are shown in Fig. S9–S10. We have also tested the Fe₁Se₁-NC catalyst structural property after the cycles. The catalyst can still maintain a two-dimensional ultrathin structure and no obvious nanoparticles or clusters are observed after cyclic testing (Fig. S11). Further observation by HAADF-STEM can directly see that Fe or Se still exists on the carbon support in the form of single atoms. Furthermore, we also provide the XPS spectrum analysis after the test. The C1s spectrum of the Fe₁Se₁-NC catalyst included three different types of species, which are C=C (284.8 eV), C=N/C=O (285.7 eV), and C-N/C=O (287.3 eV). The corresponding N1s spectrum exhibits a bimodal structure, including pyridinic N (398.4 eV), Fe-N (399.7 eV), graphitic N (400.9 eV) and oxidized N (402.4 eV). Through the Fe 2p spectrum analysis, it can also be seen that the iron mainly exists in the form of positive divalent and trivalent after the cycle reaction. The Se 3d XPS spectrum of Fe₁Se₁-NC shows a main peak at 56.0 eV, which can be assigned to C-Se-C units. Overall, after the cycle

stability test. The morphology of the catalyst and its atomic state did not change significantly. The valence state and composition of the catalyst also well maintained. These all provide strong proof of the excellent stability of the catalyst. The ORR activity of $\text{Fe}_1\text{Se}_1\text{-NC}$ was also compared with some reported catalysts in alkaline and acid solution, and it is found that $\text{Fe}_1\text{Se}_1\text{-NC}$ exhibited superior activity considering its onset potential and half-wave potential (Fig. 4H and Table S3~S4).

The anti-methanol toxicity test is another important indicator for evaluating ORR catalyst. In Fig. 5A, the current of the $\text{Fe}_1\text{Se}_1\text{-NC}$ catalyst changed slightly but recovered quickly after adding methanol. As a comparison, the Pt/C catalyst showed an obvious poisoning phenomenon with significant attenuation in current. The chronoamperometry at 0.85 V vs. RHE of $\text{Fe}_1\text{Se}_1\text{-NC}$ catalyst displayed that the ORR current maintains 91% after over 8 h continuous reaction. However, the commercialized Pt/C catalyst has a greater attenuation (ORR current only maintains 63% in 4.5 h) (Fig. 5B).

3.3. ^{57}Fe Mössbauer spectroscopy measurements

^{57}Fe Mössbauer spectroscopy was performed to further clarify the mechanism for enhanced ORR activity. It has extremely high energy resolving power for identifying the physical and chemical environment change in atomic nuclear energy level [54,55]. As shown in Fig. 6A-B, we have not observed the signals of other possible Fe-related species (e.g. Fe_xC , Fe_xO , and Fe_xSe), indicating that the iron exist in the form of atomically dispersed Fe. According to the fitting parameters (main about isomer shift (IS) and quadrupole splitting (QS) values) (Table S2), which is very sensitive to the chemical environment of Fe nuclei, three pairs of different double peaks (D1-D3) can be determined. D1, which has relatively larger values of IS (0.5–0.7) and QS (~ 3.2), can be assigned to medium-spin (MS) Fe^{2+} [56]. D2 is also classified to MS Fe^{2+} with an IS value of ~ 0.5 and a QS value of 1.1–1.3. D1 and D2 have the similar spin state, the difference is that the surrounding coordination environment may be different. Compared with D2, D3 has a low IS value and similar QS value, which can be assigned to low spin (LS) Fe^{3+} [34,55]. In Fig. 6C, it is found that the existence of Se in $\text{Fe}_1\text{-NC}$ catalyst can increase the amount of D3 (LS Fe^{3+}) content, which was further proved by DFT calculations. LS Fe^{3+} shows lower e_g filling with favorable adsorption strength of ORR intermediate products.

3.4. DFT simulation for catalytic activity

In order to further understand the catalytic performance of the $\text{Fe}_1\text{-N}_4\text{C}$, $\text{Fe}_1\text{-N}_5\text{C}$ and $\text{Fe}_1\text{Se}_1\text{-N}_5\text{C}$ for the ORR process, we inspected the value change of Gibbs free energy (Fig. 7A) along the ORR pathway (Fig. 7F). The calculation results demonstrated that the Fe site on $\text{Fe}_1\text{-N}_4\text{C}$ prefers to strongly adsorb the ORR intermediate species ($^*\text{O}$ and $^*\text{OH}$), which meaning that the Fe site on $\text{Fe}_1\text{-N}_4\text{C}$ be likely oxidized to

FeOH or FeO species rather than catalytic ORR [57]. The PDS (potential-determining step) of Fe site on $\text{Fe}_1\text{-N}_4\text{C}$ is the desorption of $^*\text{OH}$ and $\Delta G = 0.82$ eV. Furthermore, for the $\text{Fe}_1\text{-N}_5\text{C}$ system, the value change of Gibbs free energy for formation of $^*\text{OOH}$ is 0.54 eV, which is higher than the $^*\text{OH}$ desorption process (0.23 eV, the first step of the elementary reaction in the ORR $2e^-$ mechanism). While on $\text{Fe}_1\text{Se}_1\text{-N}_5\text{C}$ surface, the $^*\text{OH}$ desorption process (0.28 eV) is higher than the $^*\text{OOH}$ formation (0.22 eV), exhibiting that this Fe site is the most favorable moiety for ORR. The outstanding performance has been attributed on the appropriate Bader charge and spin density value (Fig. 7B), because the appropriate Bader charge and spin density value will lead to modestly strength adsorption of intermediate species of ORR. The charge density difference diagram shows the electron drifts from Fe to adsorbed intermediates, where OOH, O, and OH act as the charge acceptors on the TM@Grs (Fig. 7C). The pronounced delocalization indicates a significant charge transfer between the coordinated Fe atom and adsorption molecules, illustrating an obvious interaction. Fig. 7F display the possible ORR process for the $\text{Fe}_1\text{Se}_1\text{-NC}$ system. The electron occupation has changed significantly (Fig. 7D), compared with the PDOS for Fe_d orbitals before and after dopant on the Se. In $\text{Fe}_1\text{Se}_1\text{-N}_5\text{C}$ system, the Fe_d orbital overlapping becomes smaller with N_p , thus adjustment the interaction between Fe and ORR intermediates. Moreover, for the $\text{Fe}_1\text{Se}_1\text{-NC}$ and $\text{Fe}_1\text{Se}_1\text{-N}_5\text{C}$ systems, the spin-up and spin-down have significantly distinction, meaning that the spin polarization configuration of Fe be reassigned by the Se-doped.

4. Conclusion

In summary, we have developed a simple approach to prepare Fe/Se dual atoms active sites on N-doped ultrathin carbon carrier for the first time. XAFS analysis indicated that $\text{Fe}_1\text{Se}_1\text{-NC}$ catalyst mainly contains unsymmetrical coordination Fe-N_5 moiety and SeC_2 dual active sites exist. The experimental results show that the enhancement of oxygen reduction activity is mainly due to the synergistic effect of dual active sites. Furthermore, DFT calculations also indicate that the co-exist of Fe-N_5 moiety and SeC_2 dual active sites is more beneficial to $^*\text{OH}$ desorption process. This work provides a reliable designing rule of dual-atom catalysts by introducing non-metal atomic active sites for more effective ORR catalysts.

CRediT authorship contribution statement

Zhaoyang Chen and Yueming Zhai Conceived and designed the project. Xiaozhi Su Performed the X-ray absorption experiments. Zhaoyang Chen, Jie Ding, Qinye He, Zhiming Wei, Qiao Zhang, Jian Huang and Yueming Zhai performed the electrochemical experiments and analyzed the electrochemical data. Zhaoyang Chen, Jie Ding, Wenbin Zuo and Yueming Zhai conducted the Mössbauer

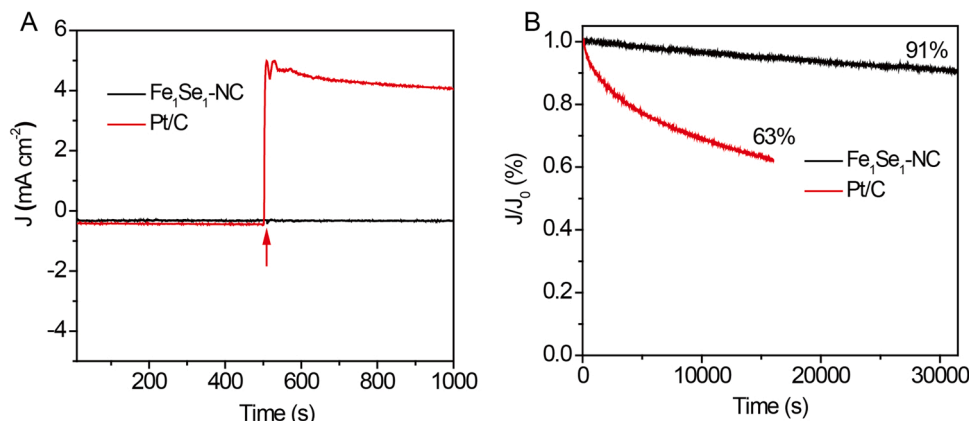


Fig. 5. A, Methanol resistance test in 0.1 M KOH electrolyte. B, Amperometric i-t curves of $\text{Fe}_1\text{Se}_1\text{-NC}$ and Pt/C in 0.1 M KOH electrolyte at 0.85 V vs. RHE.

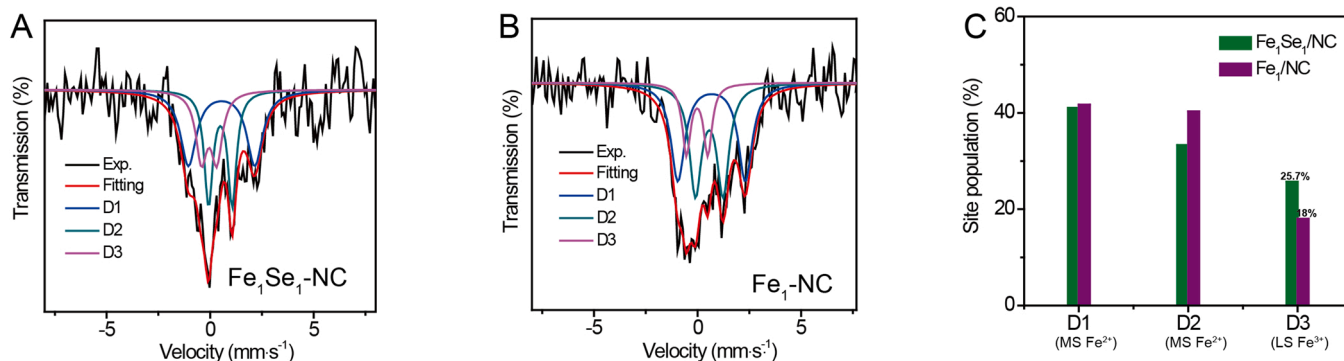


Fig. 6. A, Room-temperature ^{57}Fe Mössbauer spectroscopy measurements of $\text{Fe}_1\text{Se}_1\text{-NC}$. B, $\text{Fe}_1\text{-NC}$. C, Content of different Fe moieties of the two catalysts.

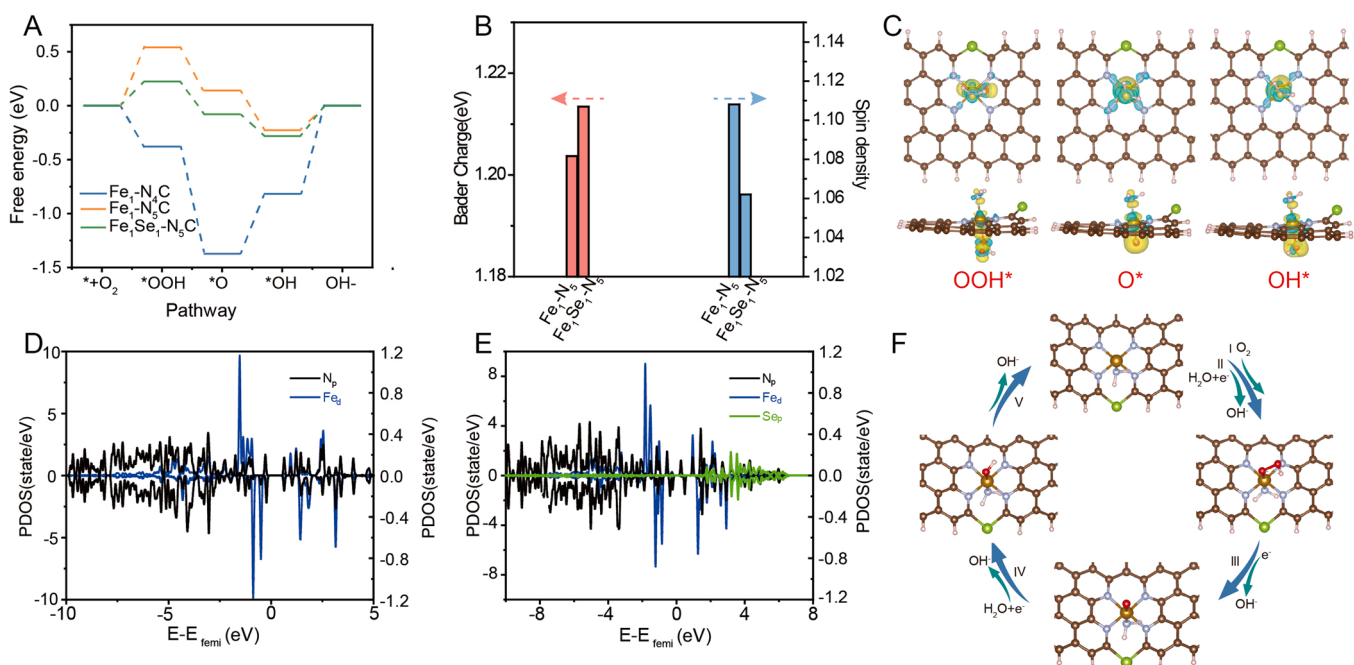


Fig. 7. A, Free-energy diagram for different Fe-centered moieties. B, The Bader charge and spin density of $\text{Fe}_1\text{Se}_1\text{-NC}$ and $\text{Fe}_1\text{-NC}$. C, Top and side views of the 3D differential charge density distributions for the three intermediate reaction steps, and the iso-surface value is 0.005 $\text{eV}/\text{\AA}^3$. D-E, The projected density of states of $\text{Fe}_1\text{-NC}$ and $\text{Fe}_1\text{Se}_1\text{-NC}$. F, The proposed ORR mechanism for the $\text{Fe}_1\text{Se}_1\text{-NC}$.

spectroscopy and analyzed the data. **Na Yang** carried out the theoretical calculations. **Zhaoyang Chen**, and **Yueming Zhai** analyzed the experimental data and prepared the manuscript. All authors reviewed and contributed to the manuscript.

Declaration of Competing Interest

The authors declare that they have no known competing financial interests or personal relationships that could have appeared to influence the work reported in this paper.

Acknowledgements

We are grateful for the financial support from National Natural Science Foundation of China (No. 21974103) and the start-up funds of Wuhan University and the HZWTECH for providing computation facilities.

Appendix A. Supporting information

Supplementary data associated with this article can be found in the

online version at [doi:10.1016/j.apcatb.2022.121206](https://doi.org/10.1016/j.apcatb.2022.121206).

References

- [1] M.K. Debe, Electrocatalyst approaches and challenges for automotive fuel cells, *Nature* 486 (2012) 43–51.
- [2] E. Luo, Y. Chu, J. Liu, Z. Shi, S. Zhu, L. Gong, J. Ge, C.H. Choi, C. Liu, W. Xing, Pyrolyzed M–N x catalysts for oxygen reduction reaction: progress and prospects, *Energy Environ. Sci.* 14 (2021) 2158–2185.
- [3] C. Tang, B. Wang, H.F. Wang, Q. Zhang, Defect engineering toward atomic Co–N_x–C in hierarchical graphene for rechargeable flexible solid Zn–air batteries, *Adv. Mater.* 29 (2017), 1703185.
- [4] Y. Tan, Z. Zhang, Z. Lei, L. Yu, W. Wu, Z. Wang, N. Cheng, Electronic modulation optimizes OH* intermediate adsorption on Co–N_x–C sites via coupling CoNi alloy in hollow carbon nanopolyhedron toward efficient reversible oxygen electrocatalysis, *Appl. Catal. B: Environ.* (2021), 121006.
- [5] I. Staffell, D. Scamman, A.V. Abad, P. Balcombe, P.E. Dodds, P. Ekins, N. Shah, K. R. Ward, The role of hydrogen and fuel cells in the global energy system, *Energy Environ. Sci.* 12 (2019) 463–491.
- [6] B. Lim, M. Jiang, P.H. Camargo, E.C. Cho, J. Tao, X. Lu, Y. Zhu, Y. Xia, Pd–Pt bimetallic nanodendrites with high activity for oxygen reduction, *Science* 324 (2009) 1302–1305.
- [7] Y. Zhou, Y. Yu, D. Ma, A.C. Foucher, L. Xiong, J. Zhang, E.A. Stach, Q. Yue, Y. Kang, Atomic Fe dispersed hierarchical mesoporous Fe–N–C nanostructures for an efficient oxygen reduction reaction, *ACS Catal.* 11 (2020) 74–81.

- [8] M.A. Ahsan, A.R. Puente Santiago, Y. Hong, N. Zhang, M. Cano, E. Rodríguez-Castellon, L. Echegoyen, S.T. Sreenivasan, J.C. Noveron, Tuning of trifunctional NiCu bimetallic nanoparticles confined in a porous carbon network with surface composition and local structural distortions for the electrocatalytic oxygen reduction, oxygen and hydrogen evolution reactions, *J. Am. Chem. Soc.* 142 (2020) 14688–14701.
- [9] X. Wei, X. Luo, H. Wang, W. Gu, W. Cai, Y. Lin, C. Zhu, Highly-defective Fe-NC catalysts towards pH-universal oxygen reduction reaction, *Appl. Catal. B: Environ.* 263 (2020), 118347.
- [10] M. Qiao, Y. Wang, Q. Wang, G. Hu, X. Mamat, S. Zhang, S. Wang, Hierarchically ordered porous carbon with atomically dispersed FeN₄ for ultraefficient oxygen reduction reaction in proton-exchange membrane fuel cells, *Angew. Chem. Int. Ed.* 59 (2020) 2688–2694.
- [11] K. Gong, F. Du, Z. Xia, M. Durstock, L. Dai, Nitrogen-doped carbon nanotube arrays with high electrocatalytic activity for oxygen reduction, *Science* 323 (2009) 760–764.
- [12] L. Jiao, J. Li, L.L. Richard, Q. Sun, T. Stracensky, E. Liu, M.T. Sougrati, Z. Zhao, F. Yang, S. Zhong, Chemical vapour deposition of Fe–N–C oxygen reduction catalysts with full utilization of dense Fe–N₄ sites, *Nat. Mater.* (2021) 1–7.
- [13] W. Zhou, H. Su, Y. Li, M. Liu, H. Zhang, X. Zhang, X. Sun, Y. Xu, Q. Liu, S. Wei, Identification of the evolving dynamics of coordination-unsaturated iron atomic active sites under reaction conditions, *ACS Energy Lett.* 6 (2021) 3359–3366.
- [14] Y. Chen, R. Gao, S. Ji, H. Li, K. Tang, P. Jiang, H. Hu, Z. Zhang, H. Hao, Q. Qu, Atomic-level modulation of electronic density at cobalt single-atom sites derived from metal–organic frameworks: enhanced oxygen reduction performance, *Angew. Chem. Int. Ed.* 60 (2021) 3212–3221.
- [15] C. Zhu, Q. Shi, B.Z. Xu, S. Fu, G. Wan, C. Yang, S. Yao, J. Song, H. Zhou, D. Du, Hierarchically porous M–N–C (M = Co and Fe) single-atom electrocatalysts with robust MN_x active moieties enable enhanced ORR performance, *Adv. Energy Mater.* 8 (2018), 1801956.
- [16] J. Li, M. Chen, D.A. Cullen, S. Hwang, M. Wang, B. Li, K. Liu, S. Karakalos, M. Lucero, H. Zhang, Atomically dispersed manganese catalysts for oxygen reduction in proton-exchange membrane fuel cells, *Nat. Catal.* 1 (2018) 935–945.
- [17] L. Bai, Z. Duan, X. Wen, R. Si, J. Guan, Atomically dispersed manganese-based catalysts for efficient catalysis of oxygen reduction reaction, *Appl. Catal. B: Environ.* 257 (2019), 117930.
- [18] B. Qiao, A. Wang, X. Yang, L.F. Allard, Z. Jiang, Y. Cui, J. Liu, J. Li, T. Zhang, Single-atom catalysis of CO oxidation using Pt₁/FeO_x, *Nat. Chem.* 3 (2011) 634–641.
- [19] X.-F. Yang, A. Wang, B. Qiao, J. Li, J. Liu, T. Zhang, Single-atom catalysts: a new frontier in heterogeneous catalysis, *Acc. Chem. Res.* 46 (2013) 1740–1748.
- [20] S. Ding, M.J. Hülsey, J. Pérez-Ramírez, N. Yan, Transforming energy with single-atom catalysts, *Joule* 3 (2019) 2897–2929.
- [21] L. Jiao, G. Wan, R. Zhang, H. Zhou, S.H. Yu, H.L. Jiang, From metal–organic frameworks to single-atom Fe implanted N-doped porous carbons: efficient oxygen reduction in both alkaline and acidic media, *Angew. Chem. Int. Ed.* 57 (2018) 8525–8529.
- [22] X. Han, X. Ling, D. Yu, D. Xie, L. Li, S. Peng, C. Zhong, N. Zhao, Y. Deng, W. Hu, Atomically dispersed binary Co–Ni sites in nitrogen-doped hollow carbon nanocubes for reversible oxygen reduction and evolution, *Adv. Mater.* 31 (2019), 1905622.
- [23] W. Zhang, Y. Chao, W. Zhang, J. Zhou, F. Lv, K. Wang, F. Lin, H. Luo, J. Li, M. Tong, Emerging dual-atom-site catalysts for efficient energy catalysis, *Adv. Mater.* (2021), 2102576.
- [24] D. Yu, Y. Ma, F. Hu, C.C. Lin, L. Li, H.Y. Chen, X. Han, S. Peng, Dual-Sites Coordination Engineering of Single Atom Catalysts for Flexible Metal–Air Batteries, *Adv. Energy Mater.* 2101242.
- [25] X. Zhong, S. Ye, J. Tang, Y. Zhu, D. Wu, M. Gu, H. Pan, B. Xu, Engineering Pt and Fe dual-metal single atoms anchored on nitrogen-doped carbon with high activity and durability towards oxygen reduction reaction for zinc-air battery, *Appl. Catal. B: Environ.* 286 (2021), 119891.
- [26] Y. Yang, Y. Qian, H. Li, Z. Zhang, Y. Mu, D. Do, B. Zhou, J. Dong, W. Yan, Y. Qin, O-coordinated W–Mo dual-atom catalyst for pH-universal electrocatalytic hydrogen evolution, *Sci. Adv.* 6 (2020) eaba6586.
- [27] Y. Ouyang, L. Shi, X. Bai, Q. Li, J. Wang, Breaking scaling relations for efficient CO₂ electrochemical reduction through dual-atom catalysts, *Chem. Sci.* 11 (2020) 1807–1813.
- [28] J. Wang, Z. Huang, W. Liu, C. Chang, H. Tang, Z. Li, W. Chen, C. Jia, T. Yao, S.J. JotA.C.S. Wei, , Design of N-coordinated dual-metal sites: a stable and active Pt-free catalyst for acidic oxygen reduction reaction, *J. Am. Chem. Soc.* 139 (2017) 17281–17284.
- [29] F. Kong, R. Si, N. Chen, Q. Wang, J. Li, G. Yin, M. Gu, J. Wang, L.-M. Liu, X.J.A.C.B. E. Sun, Origin of hetero-nuclear Au–Co dual atoms for efficient acidic oxygen reduction, *Appl. Catal. B: Environ.* 301 (2022), 120782.
- [30] Z. Chen, X. Liao, C. Sun, K. Zhao, D. Ye, J. Li, G. Wu, J. Fang, H. Zhao, J.J.A.C.B. E. Zhang, Enhanced performance of atomically dispersed dual-site Fe–Mn electrocatalysts through cascade reaction mechanism, *Appl. Catal. B: Environ.* 288 (2021), 120021.
- [31] M. Tong, F. Sun, Y. Xie, Y. Wang, Y. Yang, C. Tian, L. Wang, H.J.A.C.I.E. Fu, Operando cooperated catalytic mechanism of atomically dispersed Cu–N₄ and Zn–N₄ for promoting oxygen reduction reaction, *Angew. Chem. Int. Ed.* 60 (2021) 2–10.
- [32] D. Zhao, P. Wang, H. Di, P. Zhang, X. Hui, L. Yin, Single semi-metallic selenium atoms on Ti₃C₂ MXene nanosheets as excellent cathode for lithium–oxygen batteries, *Adv. Funct. Mater.* (2021), 2010544.
- [33] T. Wang, Q. Wang, Y. Wang, Y. Da, W. Zhou, Y. Shao, D. Li, S. Zhan, J. Yuan, H. Wang, Atomically dispersed semimetallic selenium on porous carbon membrane as an electrode for hydrazine fuel cells, *Angew. Chem.* 131 (2019) 13600–13605.
- [34] G. Shen, R. Zhang, L. Pan, F. Hou, Y. Zhao, Z. Shen, W. Mi, C. Shi, Q. Wang, X. Zhang, Regulating the spin state of Fe^{III} by atomically anchoring on ultrathin titanium dioxide for efficient oxygen evolution electrocatalysis, *Angew. Chem. Int. Ed.* 59 (2020) 2313–2317.
- [35] Z. Chen, H. Niu, J. Ding, H. Liu, P.-H. Chen, Y.-H. Lu, Y.-R. Lu, W. Zuo, L. Han, Y. Guo, Unraveling the origin of sulfur-doped Fe–N–C single atom catalyst for enhanced oxygen reduction activity: effect of Fe-spin state tuning, *Angew. Chem. Int. Ed.* 60 (2021) 25404–25410.
- [36] J. Li, M.T. Sougrati, A. Zitolo, J.M. Ablett, I.C. Oğuz, T. Mineva, I. Matanovic, P. Atanasov, Y. Huang, I. Zenyuk, Identification of durable and non-durable FeN_x sites in Fe–N–C materials for proton exchange membrane fuel cells, *Nat. Catal.* 4 (2021) 10–19.
- [37] W.H. Press, S.A. Teukolsky, B.P. Flannery, W.T. Vetterling, Numerical recipes in Fortran 77: volume 1. volume 1 of Fortran numerical recipes: the art of scientific computing, Cambridge university press., 1992.
- [38] M. Bajdich, M. García-Mota, A. Vojvodic, J.K. Nørskov, A.T. Bell, Theoretical investigation of the activity of cobalt oxides for the electrochemical oxidation of water, *J. Am. Chem. Soc.* 135 (2013) 13521–13530.
- [39] G. Kresse, J. Furthmüller, Efficiency of ab-initio total energy calculations for metals and semiconductors using a plane-wave basis set, *Comp. Mater. Sci.* 6 (1996) 15–50.
- [40] J.P. Perdew, K. Burke, M. Ernzerhof, Generalized gradient approximation made simple, *Phys. Rev. Lett.* 77 (1996) 3865.
- [41] H. Xu, D. Cheng, D. Cao, X.C.J.N.C. Zeng, A universal principle for a rational design of single-atom electrocatalysts, *Nat. Catal.* 1 (2018) 339–348.
- [42] P.E.J.Pr.B. Blöchl, Projector augmented-wave method, *Phys. Rev. B* 50 (1994) 17953.
- [43] T. Cheng, H. Xiao, W.A.J.PotN.Ao.S. Goddard, Full atomistic reaction mechanism with kinetics for CO reduction on Cu (100) from ab initio molecular dynamics free-energy calculations at 298 K, *P. Natl. Acad. Sci.* 114 (2017) 1795–1800.
- [44] H.B. Yang, S.-F. Hung, S. Liu, K. Yuan, S. Miao, L. Zhang, X. Huang, H.-Y. Wang, W. Cai, R. Chen, Atomically dispersed Ni (I) as the active site for electrochemical CO₂ reduction, *Nat. Energy* 3 (2018) 140–147.
- [45] Z.-Y. Chen, Y.-N. Li, L.-L. Lei, S.-J. Bao, M.-Q. Wang, Z.-L. Zhao, M.-w. Xu, , Investigation of Fe₂N@carbon encapsulated in N-doped graphene-like carbon as a catalyst in sustainable zinc–air batteries, *Catal. Sci. Technol.* 7 (2017) 5670–5676.
- [46] C. Liu, Y. Wu, K. Sun, J. Fang, A. Huang, Y. Pan, W.-C. Cheong, Z. Zhuang, Z. Zhuang, Q. Yuan, Constructing FeN₄/graphitic nitrogen atomic interface for high-efficiency electrochemical CO₂ reduction over a broad potential window, *Chem* 7 (2021) 1297–1307.
- [47] F. Li, T. Li, C. Sun, J. Xia, Y. Jiao, H. Xu, Selenium-doped carbon quantum dots for free-radical scavenging, *Angew. Chem. Int. Ed.* 56 (2017) 9910–9914.
- [48] J. Gu, C.-S. Hsu, L. Bai, H.M. Chen, X. Hu, Atomically dispersed Fe₃+ sites catalyze efficient CO₂ electroreduction to CO, *Science* 364 (2019) 1091–1094.
- [49] X. Zhao, X. Yang, M. Wang, S. Hwang, S. Karakalos, M. Chen, Z. Qiao, L. Wang, B. Liu, Q. Ma, Single-iron site catalysts with self-assembled dual-size architecture and hierarchical porosity for proton-exchange membrane fuel cells, *Appl. Catal. B: Environ.* 279 (2020), 119400.
- [50] M. Wang, L. Árnadóttir, Z.J. Xu, Z. Feng, In situ X-ray absorption spectroscopy studies of nanoscale electrocatalysts, *Nano-Micro Lett.* 11 (2019) 1–18.
- [51] J. Rockenberger, U. Zum Felde, M. Tischer, L. Tröger, M. Haase, H. Weller, Near edge X-ray absorption fine structure measurements (XANES) and extended X-ray absorption fine structure measurements (EXAFS) of the valence state and coordination of antimony in doped nanocrystalline SnO₂, *J. Chem. Phys.* 112 (2000) 4296–4304.
- [52] Y. Li, X. Liu, L. Zheng, J. Shang, X. Wan, R. Hu, X. Guo, S. Hong, J. Shui, Preparation of Fe–N–C catalysts with FeN_x (x = 1, 3, 4) active sites and comparison of their activities for the oxygen reduction reaction and performances in proton exchange membrane fuel cells, *J. Mater. Chem. A* 7 (2019) 26147–26153.
- [53] R. Zhao, Z. Liang, S. Gao, C. Yang, B. Zhu, J. Zhao, C. Qu, R. Zou, Q. Xu, Puffing up energetic metal–organic frameworks to large carbon networks with hierarchical porosity and atomically dispersed metal sites, *Angew. Chem.* 131 (2019) 1997–2001.
- [54] U.I. Kramm, M. Lefèvre, N. Larouche, D. Schmeisser, J.-P. Dodelet, Correlations between mass activity and physicochemical properties of Fe/N/C catalysts for the ORR in PEM fuel cell via ⁵⁷Fe Mössbauer spectroscopy and other techniques, *J. Am. Chem. Soc.* 136 (2014) 978–985.
- [55] U.I. Kramm, L. Ni, S. Wagner, ⁵⁷Fe Mössbauer spectroscopy characterization of electrocatalysts, *Adv. Mater.* 31 (2019), 1805623.
- [56] W. Liu, L. Zhang, X. Liu, X. Liu, X. Yang, S. Miao, W. Wang, A. Wang, T. Zhang, Discriminating catalytically active FeN_x species of atomically dispersed Fe–N–C catalyst for selective oxidation of the C–H bond, *J. Am. Chem. Soc.* 139 (2017) 10790–10798.
- [57] N. Yang, L. Peng, L. Li, J. Li, Q. Liao, M. Shao, Z. Wei, Theoretically probing the possible degradation mechanisms of an FeNC catalyst during the oxygen reduction reaction, *Chem. Sci.* 12 (2021) 12476–12484.